Axial momentum gains of ions and electrons in magnetic nozzle acceleration

Kazuma Emoto,[1,a)] Kazunori Takahashi,[2] and Yoshinori Takao[3,b)]

[1]*Department of Mechanical Engineering, Materials Science, and Ocean Engineering, Yokohama National University, Yokohama 240-8501, Japan*
[2]*Department of Electrical Engineering, Tohoku University, Sendai 980-8579, Japan*
[3]*Division of Systems Research, Yokohama National University, Yokohama 240-8501, Japan*
[a)]E-mail: kazuma-emoto-vh@ynu.jp
[b)]E-mail: takao@ynu.ac.jp

Abstract

Fully kinetic simulations of magnetic nozzle acceleration were conducted to investigate the axial momentum gains of ions and electrons with electrostatic and Lorentz forces. The axial momentum gains per ion and electron are directly calculated from the kinetics of charged particles, indicating that electrons in the magnetic nozzle obtain the net axial momentum by the Lorentz force, even though they are decelerated by the electrostatic force. Whereas ions are also accelerated by the electrostatic force, the axial momentum gain of electrons increases significantly with increasing magnetic field strength and becomes dominant in the magnetic nozzle. In addition, it is clearly shown that the axial momentum gain of electrons is due to the electron momentum conversion from the radial to the axial direction, resulting in a significant increase in the thrust and exhaust velocity.

1 Introduction

Electric propulsion systems are recognised as important devices for performing space missions because of their high specific impulse [1–4]. In electric propulsion systems, ion and Hall thrusters have been successfully operated in space [5–7]. However, their lifetime is limited by the wear of the cathodes and neutralizers because they are damaged by ion sputtering [8,9]. To overcome the problem of electrode wear and extend the lifetime of electric propulsion systems, researchers have vigorously developed electrodeless plasma thrusters, which do not require cathodes and neutralizers, e.g. variable specific impulse magnetoplasma rockets [10], helicon double layer thrusters [11], and magnetic nozzle radiofrequency (rf) plasma thrusters [12]. In particular, the performance of the magnetic nozzle rf plasma thruster has increased significantly in recent years [13].

The physics of the magnetic nozzle acceleration has been investigated through experiments, analytical models, and numerical simulations [12,14–17]. Previous studies have shown that a diamagnetic effect induces an azimuthal drift current in the magnetic nozzle, which produces the Lorentz force and

gives thrust to the thruster system [18–22]. More recently, the effects of drift currents on the magnetic nozzle were analysed using a fully kinetic simulation, indicating that the main drift that produced the Lorentz force was the diamagnetic effect with a strong magnetic field strength [23].

The forces exerted on ions $\boldsymbol{f}_{\mathrm{i}}$ and electrons $\boldsymbol{f}_{\mathrm{e}}$ in the electromagnetic propulsion system are generally written as

$$\boldsymbol{f}_{\mathrm{i}} = qn_{\mathrm{i}}\boldsymbol{E}, \tag{1}$$

$$\boldsymbol{f}_{\mathrm{e}} = -en_{\mathrm{e}}\boldsymbol{E} + \boldsymbol{j}_{\mathrm{e}} \times \boldsymbol{B}, \tag{2}$$

where q is the charge of the ions; e is the elementary charge; n_{i} and n_{e} are the ion and electron number densities, respectively; $\boldsymbol{j}_{\mathrm{e}}$ is the electron current density; $\boldsymbol{E}$ is the electric field; and $\boldsymbol{B}$ is the magnetic field [1]. Here, the Lorentz force exerted on ions can be neglected because the ion current density is small and the Lorentz force is sufficiently smaller than the electrostatic force [22].

In the case of Hall thrusters, the electron current density $\boldsymbol{j}_{\mathrm{e}}$ that generates the Lorentz force is due to the $\boldsymbol{E} \times \boldsymbol{B}$ effect, i.e. the Hall current [1]. The electrostatic and Lorentz forces exerted on electrons are balanced, and the net force exerted on electrons $\boldsymbol{f}_{\mathrm{e}}$ is theoretically equal to zero. Therefore, the electrons in the Hall thrusters do not obtain the net momentum. Instead of electrons, only ions are accelerated by the electrostatic force and obtain the net axial momentum directed downstream.

In the magnetic nozzle rf plasma thrusters, the Lorentz force is also exerted on electrons like in Hall thrusters. However, the electron current density that produces the Lorentz force is due to the diamagnetic effect, as reported in [19–23]. As a result, the force exerted on electrons in the magnetic nozzle is generally not zero because the electrostatic force $-en_{\mathrm{e}}\boldsymbol{E}$ is not parallel to the Lorentz force $\boldsymbol{j}_{\mathrm{e}} \times \boldsymbol{B}$ and these forces are not cancelled out. Therefore, electrons in the magnetic nozzle can obtain the net momentum by the electrostatic and Lorentz forces.

Previous studies have shown that the Lorentz force in the magnetic nozzle increases with increasing magnetic field strength [22,23]. When the magnetic field strength is sufficiently strong and the Lorentz force exceeds the electrostatic one ($|\boldsymbol{j}_{\mathrm{e}} \times \boldsymbol{B}| > |en_{\mathrm{e}}\boldsymbol{E}|$), electrons in the magnetic nozzle would obtain the net momentum in the downstream direction by the Lorentz force, while the electrostatic force decelerates the electrons. In this situation, both ions and electrons can obtain the net momentum in the downstream direction. Previous thruster models have shown that the thrust corresponding to the total axial momentum of the ions and the electrons increases along the magnetic nozzle [19, 24]. However, it has not been clearly revealed as to which particles (ions or electrons) gain the main axial momentum.

Previous studies have shown that a spontaneous electrostatic force does not impart the net momentum to the plasma and only converts the electron pressure to the ion momentum [24, 25]. However, it was also reported that the Lorentz force exerted on electrons in the magnetic nozzle imparted the net axial momentum to the plasma [21]. Although the detailed spatial measurement of the momentum change has been investigated in an experiment [26], it is still unclear how the momentums of ions and electrons are affected by the Lorentz force.

To investigate the ion and electron momentums in the magnetic nozzle, we need to obtain the electrostatic and Lorentz forces independently and analyse the momentum gains of ions and electrons given by these forces. In this study, we conducted particle-in-cell simulations of the magnetic nozzle acceleration with Monte Carlo collisions (PIC-MCCs), which treat the kinetics of both ions and electrons and the electrostatic field generated by these particles. Here, PIC-MCC simulations

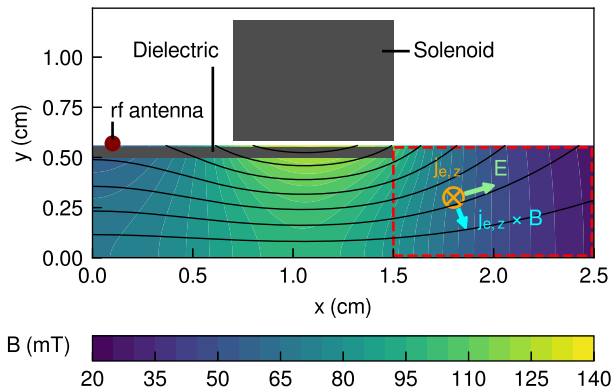

Figure 1: A schematic of the calculation area and a magnetic field strength produced by the solenoid at I_B = 2.0 kA. Solid black lines show the magnetic field lines. Figure 8 and subsequent figures are shown within a red-dotted rectangle area to focus on the magnetic nozzle acceleration, although the entire calculation area is 2.5 cm × 0.56 cm.

can investigate the momentum gains of ions and electrons independently, whereas the previous model treated the electromagnetic thrust as the sum of the ion and electron momentums [19]. The distributions of the electrostatic and Lorentz forces and the momentum gains per ion and electron are shown in section 3. We clarify the dominant force in the magnetic nozzle and determine whether it is ions or electrons that mainly obtain the net axial momentum.

2 Numerical model

We employ a two-dimensional and symmetric calculation model of a magnetic nozzle rf plasma thruster to avoid the central anomaly and reduce the calculation cost. This symmetric model simulates the bidirectional thruster, which is expected to be used for space debris removal [27]. Although the thrust balance differs between the normal unidirectional and bidirectional thrusters employed in this study, the essential plasma dynamics in the magnetic nozzle acceleration are not affected by such a symmetric configuration. Note that the two-dimensional model neglects the effect of the centrifugal force reported in [28].

Figure 1 shows a schematic of the calculation area employed in the PIC-MCC simulation. The calculation area is 2.5 cm × 0.56 cm including the dielectric. The calculation model is roughly one-sixth the size of the experiment and consists of an rf antenna, a dielectric, and a solenoid [27]. The calculation model is symmetric with respect to $x = 0$ and $y = 0$ and has an infinite length in the z-direction. The magnetic nozzle is generated by the solenoid and accelerates the plasma generated by the inductively coupled mode. The electrostatic field $\boldsymbol{E}_{\mathrm{es}}$ and the Lorentz force $\boldsymbol{j}_{\mathrm{e}} \times \boldsymbol{B}$ are exerted on the plasma in the magnetic nozzle. Figure 8 and subsequent figures are shown within a red-dotted rectangle area in figure 1 to focus on the magnetic nozzle acceleration.

The PIC-MCC simulation consists of the kinetics of the charged particles, an electrostatic field $\boldsymbol{E}_{\mathrm{es}}$, the electromagnetic field induced by the rf antenna $\boldsymbol{E}_{\mathrm{em}}$, and the magnetostatic field produced by the solenoid $\boldsymbol{B}$. The details of the PIC-MCC simulation were described in our previous papers; therefore, we only briefly describe the numerical model in this paper [23, 29, 30]. Our previous study

showed that the PIC-MCC model reproduced well the plasma profiles and the diamagnetic effect measured in previous experiments [23]. The equations of motion of charged particles are solved using the Boris method [31]. Particles are specularly reflected on the x- and y-axes because of the symmetric configuration, whereas they are simply eliminated at $x = 2.5$ cm and $y = 0.56$ cm. In addition, particles colliding with the dielectric wall are eliminated from the simulation and accumulated as a surface charge, which are used in the calculation of the electrostatic field. In this PIC-MCC simulation, we calculated the elastic, excitation, and ionisation collisions using the null-collision method [32]. The electrostatic field $\boldsymbol{E}_{\mathrm{es}}$ is obtained from the Poisson equation by using fast Fourier transformation with the Dirichlet boundary condition of $\phi = 0$ at $x = 2.5$ cm and $y = 0.56$ cm and the Neumann boundary conditions of $\partial\phi/\partial x = 0$ at $x = 0$ and $\partial\phi/\partial y = 0$ at $y = 0$, where ϕ is the potential. When solving the Poisson equation, we consider the charged particles in the bulk region, the surface charge density on the dielectric wall, and the polarisation charge on the dielectric wall as the charge density. When solving the electromagnetic field induced by the rf antenna E_{em}, the calculation area is set to 1.5 cm $\times$ 0.5 cm. E_{em} is obtained from Maxwell's equations by using fast Fourier transformation with the Dirichlet boundary condition of $E_{\mathrm{em}} = 0$ at $y = 0$ and the Neumann boundary condition of $\partial E_{\mathrm{em}}/\partial x = 0$ at $x = 0$. E_{em} on the dielectric wall at $y = 0.5$ cm and the right boundary at $x = 1.5$ cm are calculated from the plasma current and the rf current using the Biot-Savart law. The Biot-Savart law for the complex electric field $\tilde{E}_{\mathrm{em}}$ and the complex current $\tilde{I}$ is written as

$$\tilde{E}_{\mathrm{em}} = -\frac{i\omega\mu_0\tilde{I}}{4\pi}\int\frac{d\boldsymbol{l}}{|\boldsymbol{r}|}. \tag{3}$$

where i is the imaginary unit, ω is the rf angluar frequency, μ_0 is the vacuum permittivity, $\boldsymbol{l}$ is the length of the current element, and $\boldsymbol{r}$ is the position. In the two-dimensional model, equation (3) can be analytically solved, and $\tilde{E}_{\mathrm{em}}(x, y)$ on the dielectric can be written as

$$\tilde{E}_{\mathrm{em}}(x, y) = \frac{i\omega\mu_0\tilde{I}(X, Y)}{4\pi}\log\left(\frac{(x - X)^2 + (Y - y)^2}{(x - X)^2 + (Y + y)^2}\right). \tag{4}$$

where X and Y are the position of the current I. Equation (4) is calculated for all current components defined at each grid, and the sum of $\tilde{E}_{\mathrm{em}}$ is obtained by integrating them. The solenoid magnetic field $\boldsymbol{B}$ is obtained from Maxwell's equations by using fast Fourier transformation in a calculation area that is 10 times larger. Here, the solenoid current is set to 0, 0.4, and 2.0 kA to investigate the dependence of the magnetic field strength. Note that a solenoid current of 0 kA indicates no magnetic field in comparison with the magnetic nozzle acceleration. Figure 1 also shows the solenoid magnetic field strength for the solenoid current of 2.0 kA as a colour map and the magnetic field lines as solid black lines.

Table 1 shows a summary of the calculation conditions employed in our PIC-MCC simulation. The calculation area is divided into 50 μm $\times$ 50 μm cells. The cell size is determined by the Debye length and the Larmor radius. The Debye length becomes approximately 52.6 μm for the plasma density of 10^{17} m^{-3} and the electron temperature of 5 eV. In addition, the Larmor radius becomes approximately 85 μm for the magnetic field strength of 100 mT (the 2.0-kA case) and the electron temperature of 5 eV. To apply a smaller cell size than the Debye length and the Larmor radius, we chose 50 μm in the simulations. We put a hundred ions and electrons per cell as the initial particles. The rf is set to 80 MHz, and the rf current is controlled to ensure that the power absorption by the charged particle is 3.5 W/m. We treat singly charged xenon ions Xe^+ and electrons e^- as charged particles. The time step of

Table 1: Calculation conditions.

Cell size	50 μm
rf frequency	80 MHz
Power absorption	3.5 W/m
Particle	Xe^+ and e^-
Time step for ions	0.125 ns (1/100 of the rf period)
Time step for electrons	3.57 ps (1/35 the time step for ions)
Neutral density	2.0×10^{19} m^{-3}
Neutral temperature	300 K
Electron-neutral collisions	Elastic, excitation, and ionisation

the ions is set to 0.125 ns (1/100 of the rf period), and that of the electrons is set to 3.57 ps (1/35 of the time step of the ions). Neutrals are set to constant spatiotemporally as the neutral density of 2.0×10^{19} m^{-3} and the neutral temperature of 300 K. For the above-mentioned numerical configurations, the radial (y) profile of the plasma density is bimodal for the strong magnetic field case, as observed in an earlier simulation [23] and in an experiment [33], whereas it has a central peak for a weak magnetic field.

The electrostatic force $f_{\mathrm{E},x}$ and the Lorentz force $f_{\mathrm{L},x}$ exerted on an electron in the x-direction can be respectively written as

$$f_{\mathrm{E},x} = -eE_{\mathrm{es},x}, \tag{5}$$

$$f_{\mathrm{L},x} = eB_y \frac{\sum_k v_{\mathrm{e},k,z}}{N}, \tag{6}$$

where k is the index of the particles, N is the number of particles in a cell, and $v_{\mathrm{e},k,z}$ is the velocity of electron k in the z-direction, which is equivalent to the azimuthal direction in a cylindrical coordinate. Here, the electrostatic force exerted on a singly charged ion is written as $-f_{\mathrm{E},x} = eE_{\mathrm{es},x}$ because the Lorentz force exerted on ions can be negligible, as mentioned in section 1.

The momentums of the charged particles in the magnetic nozzle are changed by the electrostatic and Lorentz forces in equations (5) and (6). Here, we respectively define the momentum gains per particle in the x-direction $\Delta\dot{M}_x$ and y-direction $\Delta\dot{M}_y$ as

$$\Delta\dot{M}_x = \frac{\sum_T \sum_k \Delta(m_k v_{k,x})}{NT}, \tag{7}$$

$$\Delta\dot{M}_y = \frac{\sum_T \sum_k \Delta(m_k v_{k,y})}{NT}, \tag{8}$$

where T is the time span and $\Delta(m_k v_{k,x})$ and $\Delta(m_k v_{k,y})$ are the momentum gains of particle k in the x- and y-directions, respectively, for the time step Δt. The subsequent results were averaged over 30 μs, i.e. T = 30 μs for both ions and electrons. Note that the momentum gains in equations (7) and (8) do not include the momentum loss due to the electron-neutral collisions in the simulations because this study focuses on the momentum gain by the electrostatic and Lorentz forces. In addition, we respectively define the net momentum gains per particle in the x-direction $\Delta\dot{M}_{\mathrm{net},x}$ and the y-direction $\Delta\dot{M}_{\mathrm{net},y}$ as

$$\Delta\dot{M}_{\mathrm{net},x} = \Delta\dot{M}_{\mathrm{i},x} + \Delta\dot{M}_{\mathrm{e},x}, \tag{9}$$

$$\Delta\dot{M}_{\mathrm{net},y} = \Delta\dot{M}_{\mathrm{i},y} + \Delta\dot{M}_{\mathrm{e},y}, \tag{10}$$

where $\Delta\dot{M}_{\mathrm{i},x}$ and $\Delta\dot{M}_{\mathrm{e},x}$ are the momentum gains per ion and electron in the x-direction, respectively, and $\Delta\dot{M}_{\mathrm{i},y}$ and $\Delta\dot{M}_{\mathrm{e},y}$ are those in the y-direction, respectively, as calculated from equations (7) and (8), respectively.

3 Results and discussion

Figure 2 shows the x-y profiles of the electron number density for the three solenoid currents of 0, 0.4, and 2.0 kA. The electron number density increases with increasing solenoid current because the electrons are well confined by the magnetic field and are less likely to be lost to the dielectric wall and calculation boundaries. In addition, the y-profile of the electron number density for the solenoid current of 2.0 kA shows the bimodal shape, which was measured in previous experiments [33–37]. The ionization often occurs in the high electron density region, as shown in figure 3. Here, it is implied that the plasma profiles depend on the boundary conditions at the exit surface [38, 39]. However, the simulations in [38, 39] solved only the downstream region and some plasma inlet conditions were assumed, whereas both the plasma source and the downstream region were solved in this study. The bimodal plasma shape is expected to be generated independent of the boundary conditions at the exit surface.

Figure 4 shows the x-y profiles of the potential ϕ for the three solenoid currents of 0, 0.4, and 2.0 kA. The potential increases with increasing solenoid current and electron number density, and it is expected that the ions are more accelerated by the potential gradient. Figure 5 also shows the x-y profiles of the ion flow velocity in the x-direction $u_{i,x}$ for the three solenoid currents of 0, 0.4, and 2.0 kA. It can be seen in the figure that the axial ion flow velocity increases with increasing solenoid current, especially at the centre of the nozzle.

The simulation results are compared with experimental results. Figure 6 shows $\hat{y}$ profiles of the normalized electron number density $\hat{n}_{\mathrm{e}}$ and the normalized potential $\hat{\phi}$, respectively, for the solenoid current of 2.0 kA. Note that the coordinates y and the measured number density n_e and potential ϕ are normalized by their maximum values. $\hat{n}_{\mathrm{e}}$ and $\hat{\phi}$ are roughly consistent between the simulation and the experiment within $-0.5 < \hat{y} < 0.5$, whereas there are relatively large differences in $|\hat{y}| > 0.5$ because the simulation assumes the $\phi = 0$ at $\hat{y} = \pm 1.0$. Therefore, the plasma dynamics is expected to be reproduced in core region of the magnetic nozzle, although the plasma near the calculation boundary is not consistent with the experiment. The electron pressure around central axis (x-axis in this paper) is estimated to be small compared with cylindrical setup in the experiment, as written in our previous paper [23]. Note that the small pressure around the central axis increases the pressure gradient, overestimating the Lorentz force in the magnetic nozzle.

Figure 7 shows the x-y profiles of the electrostatic field in the x-direction $E_{\mathrm{es},x}$ for the three solenoid currents of 0, 0.4, and 2.0 kA. The electrostatic field in the x-direction $E_{\mathrm{es},x}$ is positive in almost the entire region because the plasma expands through the magnetic nozzle and the potential decreases in the downstream direction. It should be noted that the negative electrostatic field is observed at the peripheral region at x = 1.7–2.3 cm and $y = \pm$(0.3–0.56) cm and decreases with increasing solenoid

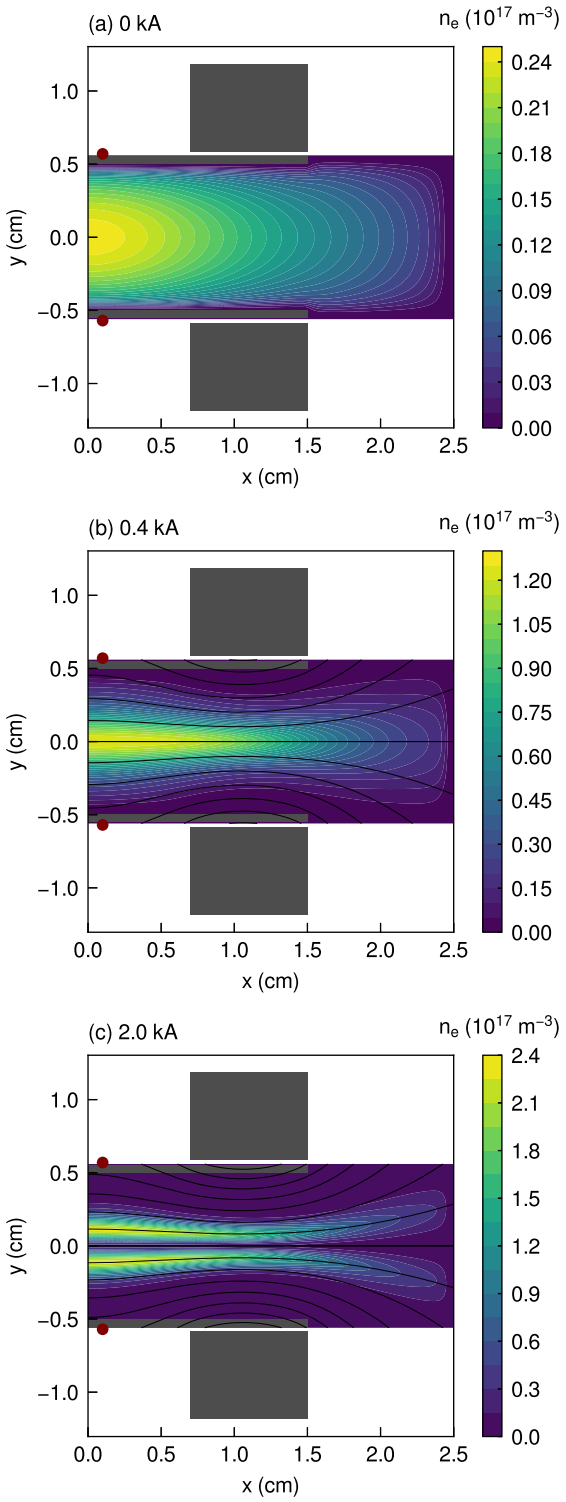

Figure 2: x-y profiles of the electron number density n_e for the three solenoid currents of (a) 0, (b) 0.4, and (c) 2.0 kA. Solid black lines show the magnetic field lines produced by the solenoid.

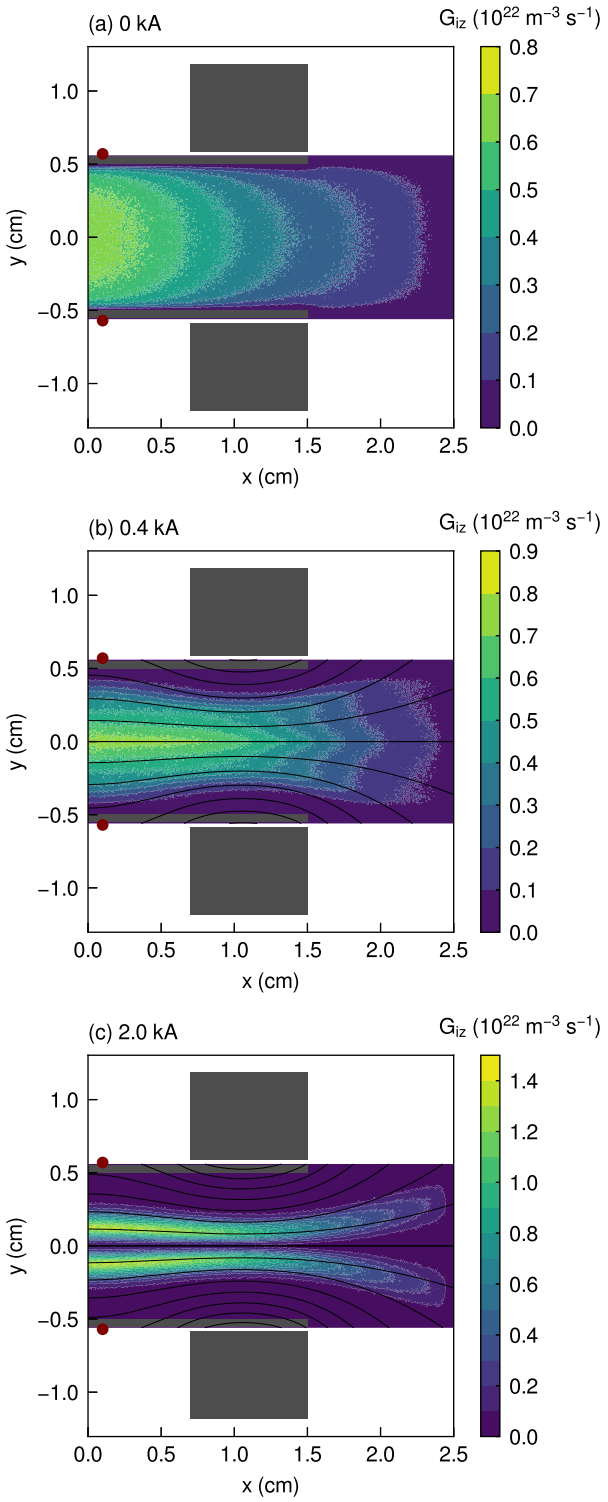

Figure 3: x-y profiles of the ionization rate G_{iz} for the three solenoid currents of (a) 0, (b) 0.4, and (c) 2.0 kA. Solid black lines show the magnetic field lines produced by the solenoid.

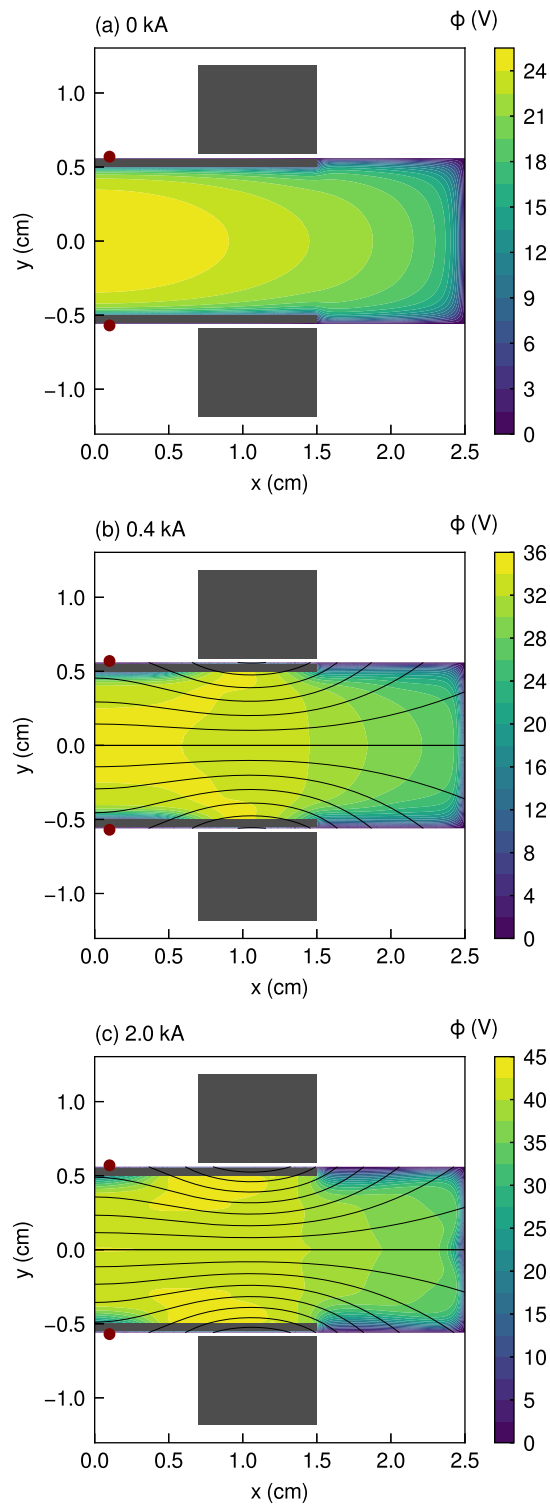

Figure 4: x-y profiles of the potential ϕ for the three solenoid currents of (a) 0, (b) 0.4, and (c) 2.0 kA. Solid black lines show the magnetic field lines produced by the solenoid.

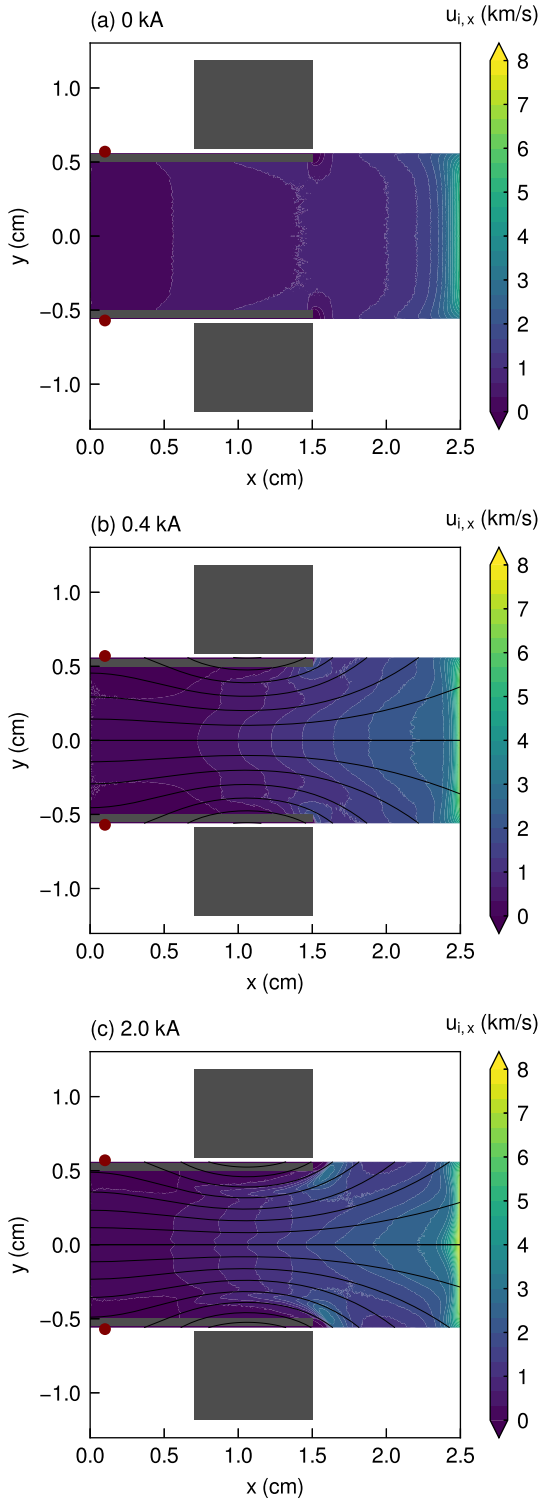

Figure 5: x-y profiles of the ion flow velocity in the x-direction $u_{i,x}$ for the three solenoid currents of (a) 0, (b) 0.4, and (c) 2.0 kA. Solid black lines show the magnetic field lines produced by the solenoid.

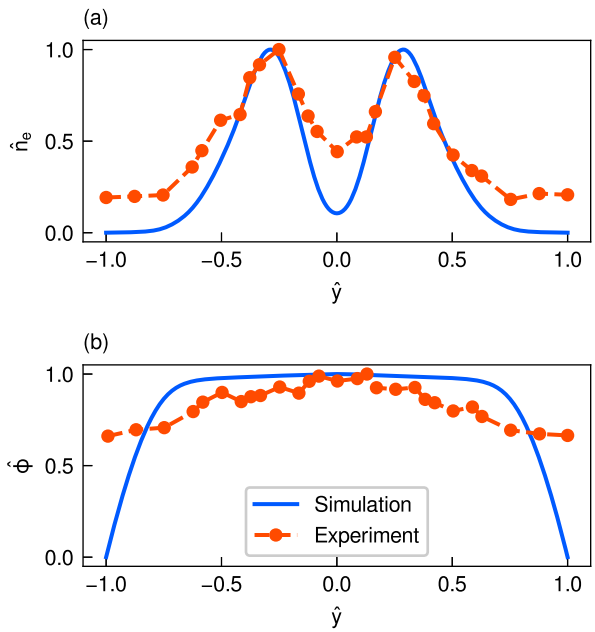

Figure 6: $\hat{y}$ profiles of (a) the normalized electron number density $\hat{n}_e$ and (b) the normalized potential $\hat{\phi}$, respectively, for the solenoid current of 2.0 kA. The coordinate y is normalized by the maximum position y_{max} as $\hat{y} = y/y_{max}$, the electron number density n_e is normalized by the maximum pressure $n_{e,max}$ as $\hat{n}_e = n_e/n_{e,max}$, and the potential ϕ is normalized by the maximum potential ϕ_{max} as $\hat{\phi} = \phi/\phi_{max}$. The simulation result is a cross-section of $x = 2.0$ cm for the 2.0 kA case, and the experimental result is a cross-section of $z = 5$ cm for the 12 A case in Ref. 22.

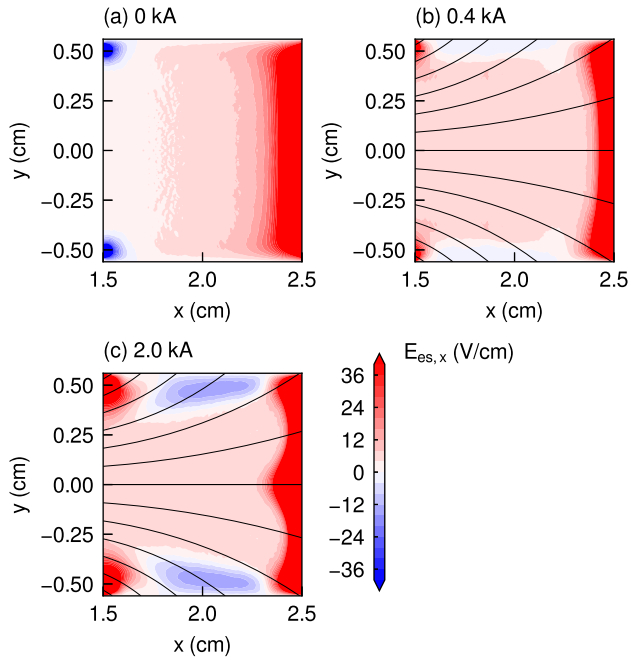

Figure 7: x-y profiles of the electrostatic field in the x-direction $E_{\mathrm{es},x}$ for the three solenoid currents of (a) 0, (b) 0.4, and (c) 2.0 kA. Solid black lines show the magnetic field lines produced by the solenoid.

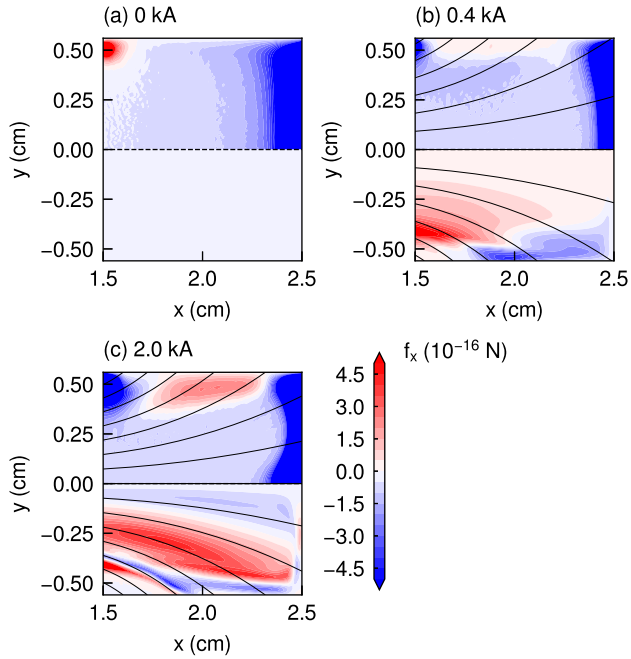

Figure 8: x-y profiles of the electrostatic force $f_{\mathrm{E},x}$ (upper half) and the Lorentz force $f_{\mathrm{L},x}$ (lower half) exerted on an electron in the x-direction for the three solenoid currents of (a) 0, (b) 0.4, and (c) 2.0 kA. Solid black lines show the magnetic field lines produced by the solenoid.

current, especially for the case of the 2.0-kA solenoid current. This negative electrostatic field implies that the high potential is formed in the plasma core flowing along the divergent magnetic field lines. The electron number density at approximately $|y| > 0.3$ cm decreases in the negative x-direction, as shown in figures 2(b) and 2(c), resulting in the potential gradient being directed to the positive x-direction and the negative electrostatic field.

Figure 8 shows the x-y profiles of the electrostatic force $f_{\mathrm{E},x}$ (upper half) and the Lorentz force $f_{\mathrm{L},x}$ (lower half) exerted on an electron in the x-direction for the three solenoid currents of 0, 0.4, and 2.0 kA. It should be noted that the sheath is generated at $x = 2.3$–2.5 cm and $y = \pm(0.4$–$0.56)$ cm because the electrostatic field $\boldsymbol{E}_{\mathrm{es}}$ is solved with the Dirichlet boundary condition as $\phi = 0$. Here, the Lorentz force for the solenoid current of 0 kA is zero, as seen in figure 8(a), because of the absence of the magnetic field.

The electrostatic force exerted on an electron $f_{\mathrm{E},x}$ is negative in almost the entire region, and its magnitude is not significantly changed by the solenoid current. As a result, the electrostatic force $f_{\mathrm{E},x}$ decelerates the electrons expanding through the magnetic nozzle and, instead, accelerates the ions in the downstream direction. The Lorentz force exerted on an electron $f_{\mathrm{L},x}$ increases dramatically with increasing solenoid current, clearly exceeding the electrostatic force $f_{\mathrm{E},x}$ for the solenoid current of 2.0 kA. A negative Lorentz force also exists at the centre of the magnetic nozzle in figure 8(c), which is due to the bimodal plasma shape in figure 2(c), as reported in [23]. The bimodal plasma shape forms a hollow region within the maximum electron number density and around $y = 0$ cm. In this hollow region, diamagnetic drift currents are induced, whose directions are $+z$ at $x > 0$ cm and $-z$ at $x < 0$ cm. These currents also induce a negative Lorentz force with the solenoid magnetic field, as shown in figure 2(c). The positive Lorentz force accelerates the electrons in the downstream direction, whereas the electrostatic force decelerates them.

Figure 9 shows the x-y profiles of the axial momentum gains per ion $\Delta\dot{M}_{\mathrm{i},x}$ and electron $\Delta\dot{M}_{\mathrm{e},x}$ for the solenoid current of 0 kA, which are directly calculated from the velocities of the ions and the electrons, as described in equation (7). The net axial momentum gain per particle $\Delta\dot{M}_{\mathrm{net},x}$ is also calculated, which is the sum of $\Delta\dot{M}_{\mathrm{i},x}$ and $\Delta\dot{M}_{\mathrm{e},x}$, as shown in equation (9). It should be noted that the magnitudes of the axial momentum gains per ion and electron are large at $x = 2.3$–2.5 cm because of the sheath. The axial momentum gain per ion $\Delta\dot{M}_{\mathrm{i},x}$ is positive in almost the entire region, indicating that ions obtain the momentum in the x-direction and are accelerated in the downstream direction by the electrostatic field. However, the axial momentum gain per electron $\Delta\dot{M}_{\mathrm{e},x}$ is negative in almost all regions. Whereas low-energy electrons are reflected by the sheath, energetic electrons are decelerated by the electrostatic field and lose the momentum at the boundary. The net axial momentum gain per particle $\Delta\dot{M}_{\mathrm{net},x}$ is almost zero, as shown in figure 9(c); therefore, the axial momentum gains per ion and electron cancel each other out. This result is consistent with the analytical prediction in [24] and with the experiment results in [40, 41]. Figure 10 shows the y profile of the axial momentum gains per particle for the solenoid current of 0 kA at $x = 1.8$ cm. The axial momentum gains per ion and electron are symmetric, and the net axial momentum gain per particle $\Delta\dot{M}_{\mathrm{net},x}$ is completely zero. Therefore, the results of our PIC-MCC simulation shows that the plasma without the magnetic field does not obtain the net momentum, as reported in [24].

Figures 11 and 12 show the x-y profiles of the axial momentum gains per ion $\Delta\dot{M}_{\mathrm{i},x}$ and electron $\Delta\dot{M}_{\mathrm{e},x}$ for the two solenoid currents of 0.4 and 2.0 kA, respectively. The net axial momentum gain per particle $\Delta\dot{M}_{\mathrm{net},x}$ is also calculated, which is the sum of $\Delta\dot{M}_{\mathrm{i},x}$ and $\Delta\dot{M}_{\mathrm{e},x}$, as shown in equation (9). It should be noted that the region at $x = 2.3$–2.5 cm and $y = \pm(0.4$–$0.56)$ cm contains the effect of the sheath near the boundaries. The axial momentum gain per ion $\Delta\dot{M}_{\mathrm{i},x}$ is positive in almost the entire

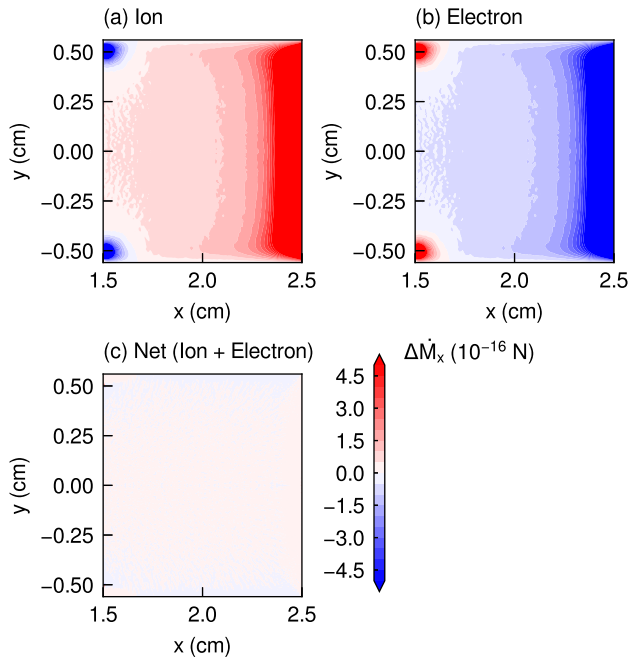

Figure 9: x-y profiles of the axial momentum gains per (a) ion $\Delta\dot{M}_{\mathrm{i},x}$ and (b) electron $\Delta\dot{M}_{\mathrm{e},x}$ for the solenoid current of 0 kA. The net momentum gain per particle $\Delta\dot{M}_{\mathrm{net},x}$ is also shown in (c), which is the sum of $\Delta\dot{M}_{\mathrm{i},x}$ and $\Delta\dot{M}_{\mathrm{e},x}$.

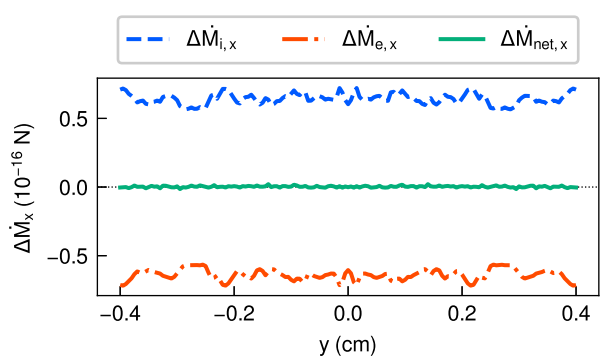

Figure 10: y profile of the axial momentum gain per ion $\Delta\dot{M}_{\mathrm{i},x}$ (a dashed blue line) and electron $\Delta\dot{M}_{\mathrm{e},x}$ (a dashed-dotted orange line) for the solenoid current of 0 kA at x = 1.8 cm. The net momentum gain per particle $\Delta\dot{M}_{\mathrm{net},x}$ (a solid green line) is also plotted, which is the sum of $\Delta\dot{M}_{\mathrm{i},x}$ and $\Delta\dot{M}_{\mathrm{e},x}$. The data for $|y| > 0.4$ cm are eliminated because they are affected by the sheath due to the finite calculation area.

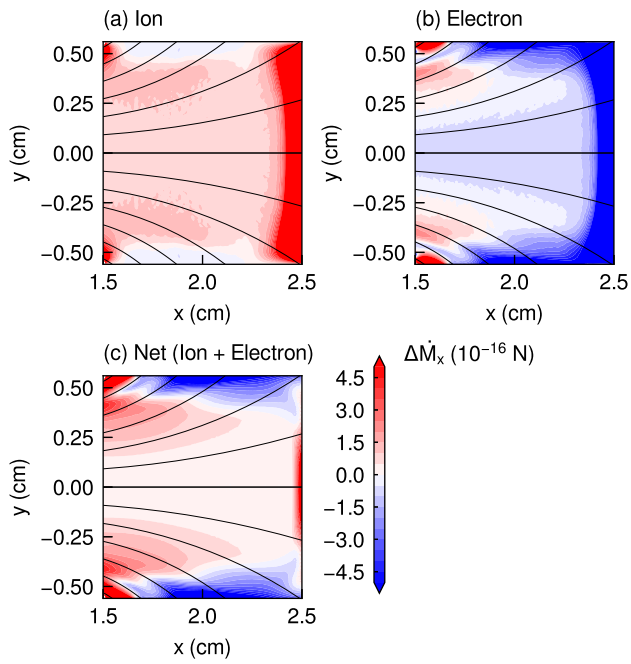

Figure 11: x-y profiles of the axial momentum gains per (a) ion $\Delta\dot{M}_{\mathrm{i},x}$ and (b) electron $\Delta\dot{M}_{\mathrm{e},x}$ for the solenoid current of 0.4 kA. The net axial momentum gain per particle $\Delta\dot{M}_{\mathrm{net},x}$ is also shown in (c), which is the sum of $\Delta\dot{M}_{\mathrm{i},x}$ and $\Delta\dot{M}_{\mathrm{e},x}$. Solid black lines show the magnetic field lines produced by the solenoid.

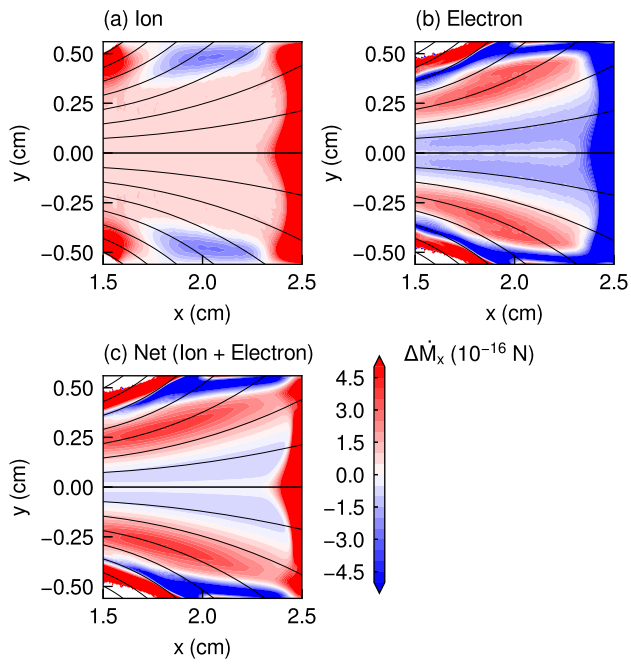

Figure 12: x-y profiles of the axial momentum gains per (a) ion $\Delta\dot{M}_{\mathrm{i},x}$ and (b) electron $\Delta\dot{M}_{\mathrm{e},x}$ for the solenoid current of 2.0 kA. The net axial momentum gain per particle $\Delta\dot{M}_{\mathrm{net},x}$ is also shown in (c), which is the sum of $\Delta\dot{M}_{\mathrm{i},x}$ and $\Delta\dot{M}_{\mathrm{e},x}$. Solid black lines show the magnetic field lines produced by the solenoid.

region regardless of the two solenoid currents, as shown in figures 11(a) and 12(a); therefore, ions obtain the axial momentum and are accelerated by the electrostatic force. The axial momentum gain per electron $\Delta\dot{M}_{\mathrm{e},x}$ is almost negative for the solenoid current of 0.4 kA, whereas the positive axial momentum gain per electron also exists on the magnetic field line passing through x = 1.5 cm and y = ±0.35 cm, indicating that the electron momentum increases by the Lorentz force and exceeds the electrostatic force around there. For the solenoid current of 2.0 kA, the positive axial momentum gain per electron clearly exists on the magnetic field line passing through x = 1.5 cm and y = ±0.25 cm, whereas the negative axial momentum gain per electron also exists at the centre of the magnetic nozzle. Regions where the positive axial momentum gain per electron exists are consistent with the locations where the Lorentz force in the x-direction is exerted on electrons, as shown in figure 8(c). In this region, the Lorentz force exceeds the electrostatic one and accelerates the electrons in the downstream direction, even though the electrostatic force decelerates them. At the centre of the magnetic nozzle, the negative axial momentum gain per electron exists for the solenoid current of 2.0 kA because both the electrostatic and Lorentz forces exerted on electrons are negative, as shown in figure 8(c). In this region, electrons are decelerated by both the electrostatic and Lorentz forces.

As shown in figures 11(c) and 12(c), the net axial momentum gain per particle $\Delta\dot{M}_{\mathrm{net},x}$ is not zero, unlike in the case without the magnetic field shown in figure 9(c). This is consistent with the results of a previous study [21] where the magnetic nozzle imparts the net momentum to the plasma. In this situation, the plasma momentum is converted not only by the spontaneous electric field but also by the Lorentz force with the magnetic field. For the solenoid current of 0.4 kA, the net axial momentum gain per particle is positive because the axial momentum gain per electron increases by the Lorentz force and that per ion becomes dominant. For the solenoid current of 2.0 kA, however, the axial momentum gain per electron increases significantly by the Lorentz force and becomes dominant instead of the ions. These results indicate that the electron momentum imparted by the strong magnetic field exceeds the ion momentum imparted by the electrostatic field. Here, it is still unclear whether the net axial momentum gain per particle near the right boundary at x = 2.5 cm is large, where the sheath is generated because of the boundary condition. One of the possible reasons could be the generation of the $\boldsymbol{E} \times \boldsymbol{B}$ drift current due to the presence of the strong electric field in the sheath, and thus, further verification will be required to fully understand it. Because the present study focuses on the momentum gain in the core region (not in the sheath), this is beyond the scope of the present study.

Figure 13 shows the y profile of the axial momentum gains per particle for the solenoid current of 2.0 kA at x = 1.8 cm. Note that the axial momentum gains per particle at $|y| > 0.4$ cm are eliminated because they are affected by the sheath. The axial momentum gain per ion is positive and uniform at approximately 1.0×10^{-16} N within -0.3 cm $< y <$ 0.3 cm. The axial momentum gain per electron $\Delta\dot{M}_{\mathrm{e},x}$ is larger than that per ion in the outer regions of $|y| > 0.2$ cm, where the electrons are mainly accelerated by the Lorentz force in the downstream direction instead of the ions. However, the electrostatic force exceeds the Lorentz force in the inner region of $|y| < 0.2$ cm and mainly accelerates the ions in the downstream direction instead of the electrons. Here, the net axial momentum gain per particle is dominated by the axial momentum gain per electron in the outer regions of $|y| > 0.2$ cm at the strong magnetic field.

The positive axial momentum gain per electron in figure 12(b) implies that the electron energy in the x-direction increases with the magnetic nozzle. However, the magnetostatic field produced by the solenoid does not provide energy to the electrons. Therefore, the increase in the electron energy in the x-direction must be due to the energy conversion from the y- and z-directions to the x-direction.

The spontaneous electrostatic field converts the electron pressure in the x-direction to the ion

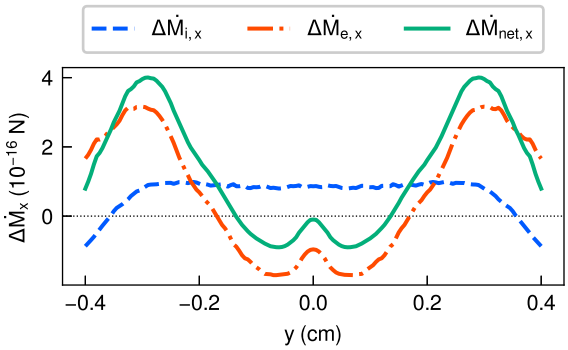

Figure 13: y profile of the axial momentum gain per ion $\Delta\dot{M}_{\mathrm{i},x}$ (a dashed blue line) and electron $\Delta\dot{M}_{\mathrm{e},x}$ (a dashed-dotted orange line) for the solenoid current of 2.0 kA at x = 1.8 cm. The net axial momentum gain per particle $\Delta\dot{M}_{\mathrm{net},x}$ (a solid green line) is also plotted, which is the sum of $\Delta\dot{M}_{\mathrm{i},x}$ and $\Delta\dot{M}_{\mathrm{e},x}$. The data for $|y| > 0.4$ cm are eliminated because they are affected by the sheath due to the finite calculation area.

momentum in the x-direction, as reported in [24]. However, the spontaneous electrostatic field does not convert the electron pressure in the y- and z-directions to the ion momentum in the x-direction. To increase the axial electron momentum without any external work, we need to convert the energy corresponding to the electron pressure in the y- and z-directions to the x-direction through the Lorentz force.

Figure 14 shows the x-y profiles of the net momentum gain per particle in the y-direction $\Delta\dot{M}_{\mathrm{net},y}$ for the solenoid currents of 0, 0.4, and 2.0 kA. Comparing figure 14 with figures 9(c), 11(c), and 12(c), we can see that the regions where the net momentum gain per particle in the y-direction increases or decreases correspond to those where the net momentum gain per particle in the x-direction decreases or increases, respectively. Here, the net momentum gain is calculated as the sum of the ion and electron momentums, and the effect of the electrostatic field is cancelled out, indicating the momentum conversion by the Lorentz force. Thus, the role of the magnetic nozzle is to convert the electron momentum in the y-direction to that in the x-direction to utilize the electron energy efficiently. Note that the net momentum gain per particle in the z-direction is confirmed to be neglected because it is calculated to be approximately two orders of magnitude smaller than those in the x- and y-directions.

The positive axial momentum gain per electron given by the Lorentz force means that electrons are accelerated in the downstream direction and are more likely to be lost to the downstream boundary. In this situation, the plasma potential would increase to prevent the loss of electrons. Figure 15 shows the x profile of the potential for the three solenoid currents of 0, 0.4, and 2.0 kA at y = 0 cm. The plasma potential on the left-hand side of figure 15 increases with increasing solenoid current, indicating that the plasma prevents the loss of electrons spontaneously. In addition, the increase in the plasma potential further accelerates the ions by the electrostatic field, resulting in an increase in the exhaust velocity.

To investigate the net thrust obtained by the magnetic nozzle, we calculated the total axial momentum gain by integrating the ion and electron momentum gains in the x-direction within 1.5 cm $< x <$ 2.3 cm and -0.35 cm $< y <$ 0.35 cm to eliminate the sheath effect. Table 2 shows the total axial momentum gain in the magnetic nozzle. For the solenoid current of 0 kA, the magnitudes of the axial momentum gains of ions and electrons are almost the same, indicating that the net axial

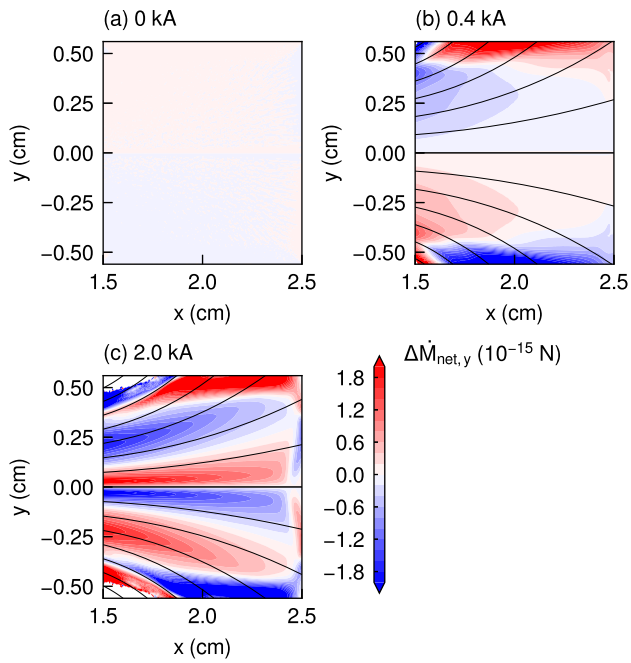

Figure 14: x-y profiles of the net momentum gain per particle in the y-direction $\Delta\dot{M}_{\mathrm{net},y}$ for the solenoid currents of (a) 0, (b) 0.4, and (c) 2.0 kA. Solid black lines show the magnetic field lines produced by the solenoid.

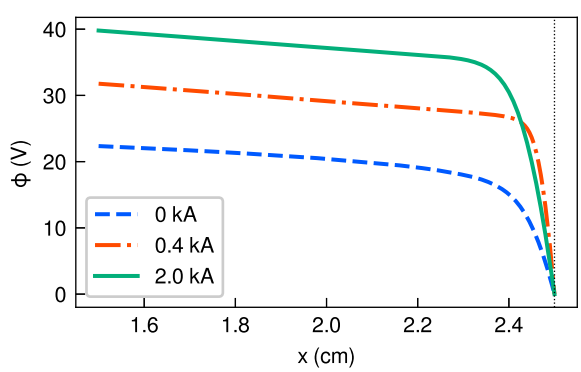

Figure 15: x profile of the potential ϕ for the three solenoid currents of 0 (a dashed blue line), 0.4 (a dashed-dotted orange line), and 2.0 kA (a solid green line) at $y = 0$ cm. The vertical dotted black line at $x = 2.5$ cm shows the right boundary of the calculation area, where the Dirichlet boundary condition of $\phi = 0$ is assumed.

Table 2: Total axial momentum gains in the magnetic nozzle, which are calculated by integrating the axial momentum gains per particle within 1.5 cm < x < 2.3 cm and −0.35 cm < y < 0.35 cm to eliminate the sheath effect.

Solenoid current (kA)	Axial momentum gain (μN/m)		
	Ion	Electron	Net (Ion + Electron)
0	16.8	−17.9	−1.13
0.4	37.1	−9.64	27.5
2.0	34.6	47.1	81.7

momentum gain becomes small. For the solenoid current of 0.4 kA, the axial momentum gains of ions and electrons increase and the net axial momentum gain also increases. For the solenoid current of 2.0 kA, the axial momentum gain of electrons increases dramatically, whereas the axial momentum gain of ions remains almost unchanged. As a result, the axial momentum gain of electrons becomes positive and exceeds that of the ions. The net axial momentum gain also increases significantly, even though a negative net axial momentum gain exists in the centre of the magnetic nozzle, as shown in figure 12(c).

These results are different from the phenomena in Hall thrusters, where the axial momentum gain per electron is theoretically zero. In the magnetic nozzle, the axial momentum gain per electron is not zero because of the Lorentz force due to the diamagnetic effect, and electrons obtain the net axial momentum, contributing to the increase in the thrust and the exhaust velocity. The magnetic nozzle has a mechanism to obtain the thrust by accelerating the electrons, where the electron momentum in the y-direction is converted to that in the x-direction.

4 Conclusion

We conducted particle-in-cell simulations of a bidirectional magnetic nozzle rf plasma thruster with Monte Carlo collisions to investigate the axial momentum gains of ions and electrons in the magnetic nozzle. The axial momentum gains per ion and electron were calculated directly from the particle velocities, and the results are discussed with the calculated electrostatic and Lorentz forces, which are exerted on ions and electrons and impart the momentum to the plasma. The Lorentz force in the x-direction increases with increasing solenoid current and exceeds the electrostatic force in the x-direction at a strong magnetic field strength. The axial momentum gain per electron is also increased dramatically by the Lorentz force and becomes dominant in the magnetic nozzle instead of ions. It is clearly shown that the increase in the electron momentum in the x-direction is due to the momentum conversion of electrons from the y- to the x-direction by the Lorentz force. The plasma potential also increases because of the loss of electrons, resulting in an increase in the exhaust velocity of the ions. Therefore, the magnetic nozzle obtains the thrust by mainly imparting the net momentum in the x-direction to the electrons.

Acknowledgement

This work was partly supported by JSPS KAKENHI Grant Numbers JP21J15345 and JP19H00663. The computer simulation was performed on the A-KDK computer system at the Research Institute for

Sustainable Humanosphere, Kyoto University. One of the authors (K.E.) received a scholarship from the Futaba Foundation.

Data Availability

The data that support the findings of this study are available upon reasonable request from the authors.

References

[1] Goebel D M and Katz I 2008 *Fundamentals of electric propulsion: ion and Hall thrusters* (John Wiley & Sons)

[2] Charles C 2009 *J. Phys. D: Appl. Phys.* **42** 163001

[3] Mazouffre S 2016 *Plasma Sources Sci. Technol.* **25** 033002

[4] Levchenko I, Xu S, Mazouffre S, Lev D, Pedrini D, Goebel D, Garrigues L, Taccogna F and Bazaka K 2020 *Phys. Plasmas* **27** 020601

[5] Racca G, Whitcomb G and Foing B 1998 *ESA bulletin* **95** 72

[6] Kuninaka H, Nishiyama K, Funaki I, Yamada T, Shimizu Y and Kawaguchi J 2007 *J. Propul. Power* **23** 544

[7] Brophy J R, Garner C E and Mikes S C 2009 *J. Propul. Power* **25** 1189

[8] Kim V 1998 *J. Propul. Power* **14** 736

[9] Goebel D M, Polk J E and Mikellides I G 2011 *J. Propul. Power* **27** 768

[10] Arefiev A V and Breizman B N 2004 *Phys. Plasmas* **11** 2942

[11] Charles C 2007 *Plasma Sources Sci. Technol.* **16** R1

[12] Takahashi K 2019 *Rev. Mod. Plasma Phys.* **3** 3

[13] Takahashi K 2021 *Sci. Rep.* **11** 2768

[14] Little J M and Choueiri E Y 2013 *Phys. Plasmas* **20** 103501

[15] Lafleur T 2014 *Phys. Plasmas* **21** 043507

[16] Williams L T and Walker M L 2015 *IEEE Trans. Plasma Sci.* **43** 1694–1705

[17] Kaganovich I D, Smolyakov A, Raitses Y, Ahedo E, Mikellides I G, Jorns B, Taccogna F, Gueroult R, Tsikata S, Bourdon A *et al* 2020 *Phys. Plasmas* **27** 120601

[18] Ahedo E and Merino M 2010 *Phys. Plasmas* **17** 073501

[19] Takahashi K, Lafleur T, Charles C, Alexander P and Boswell R W 2011 *Phys. Rev. Lett.* **107** 235001

[20] Fruchtman A, Takahashi K, Charles C and Boswell R 2012 *Phys. Plasmas* **19** 033507

[21] Takahashi K, Charles C and Boswell R W 2013 *Phys. Rev. Lett.* **110** 195003

[22] Takahashi K, Chiba A, Komuro A and Ando A 2016 *Plasma Sources Sci. Tech.* **25** 055011

[23] Emoto K, Takahashi K and Takao Y 2021 *Phys. Plasmas* accepted arXiv:2104.02854

[24] Fruchtman A 2006 *Phys. Rev. Lett.* **96** 065002

[25] Lafleur T, Charles C and Boswell R 2010 *Phys. Plasmas* **17** 043505

[26] Takahashi K, Sugawara T and Ando A 2020 *New J. Phys.* **22** 073034

[27] Takahashi K, Charles C, Boswell R W and Ando A 2018 *Sci. Rep.* **8** 14417

[28] Fisch N, Raitses Y and Fruchtman A 2011 *Plasma Phys. Control. Fusion* **53** 124038

[29] Takao Y and Takahashi K 2015 *Phys. Plasmas* **22** 113509

[30] Takase K, Takahashi K and Takao Y 2018 *Phys. Plasmas* **25** 023507

[31] Birdsall C K and Langdon A B 2004 *Plasma physics via computer simulation* (CRC press)

[32] Vahedi V and Surendra M 1995 *Comput. Phys. Comm.* **87** 179–198

[33] Takahashi K, Akahoshi H, Charles C, Boswell R W and Ando A 2017 *Phys. Plasmas* **24** 084503

[34] Takahashi K, Charles C, Boswell R, Cox W and Hatakeyama R 2009 *Appl. Phys. Lett.* **94** 191503

[35] Charles C 2010 *Appl. Phys. Lett.* **96** 051502

[36] Ghosh S, Yadav S, Barada K, Chattopadhyay P, Ghosh J, Pal R and Bora D 2017 *Phys. Plasmas* **24** 020703

[37] Gulbrandsen N and Fredriksen Å 2017 *Front. Phys.* **5** 2

[38] Rao S and Singh N 2012 *Phys. Plasmas* **19** 093507

[39] Chen Z, Wang Y, Tang H, Ren J, Li M, Zhang Z, Cao S and Cao J 2020 *Phys. Rev. E* **101** 053208

[40] Takahashi K, Lafleur T, Charles C, Alexander P, Boswell R, Perren M, Laine R, Pottinger S, Lappas V, Harle T *et al* 2011 *Appl. Phys. Lett.* **98** 141503

[41] Lafleur T, Takahashi K, Charles C and Boswell R 2011 *Phys. Plasmas* **18** 080701